energies

MDPI

Article

A Secondary-Side Controlled Electric Vehicle Wireless Charger

Fabio Corti [1,*], Alberto Reatti [1], Andrea Nepote [2], Luca Pugi [1], Marco Pierini [1], Libero Paolucci [1], Francesco Grasso [1], Emanuele Grasso [3] and Matthias Nienhause [3]

[1] Department of Information Engineering, University of Florence, 50139 Florence, Italy; alberto.reatti@unifi.it (A.R.); luca.pugi@unifi.it (L.P.); marco.pierini@unifi.it (M.P.); libero.paolucci@unifi.it (L.P.); francesco.grasso@unifi.it (F.G.)
[2] Marelli S.p.A., Venaria Reale, 10078 Torino, Italy; andrea.nepote@marelli.com
[3] Lehrstuhl für Antriebstechnik, Universität des Saarlandes, 66123 Saarbrücken, Germany; grasso@lat.uni-saarland.de (E.G.); nienhaus@lat.uni-saarland.de (M.N.)
* Correspondence: fabio.corti@unifi.it

Received: 11 November 2020; Accepted: 9 December 2020; Published: 10 December 2020

Abstract: In this paper, the design procedure of an electric vehicle (EV) wireless charger is presented. Unlike most of the systems available in the literature, the proposed charging system is regulated from the vehicle side. The on-board electrical circuit automatically adapts the resonant compensation to guarantee compatibility with the primary inverter characteristics and achieve high transmission efficiency without communication between sides. Moreover, the proposed control strategy, used to regulate the secondary full active rectifier (FAR), allows the supply of the the EV battery, maximizing the efficiency during the whole charging process.

Keywords: wireless power transfer; resonant compensations; electric vehicle; wireless charging

1. Introduction

Over the last few years, wireless power transfer (WPT) has attracted increasing interest from academia and industry for its promising application to electric vehicle charging. The embedded underground infrastructure makes the charging station less sensitive to weather conditions and vandal attacks if compared with the wired solution. Exposure to rain, snow, humidity, and temperature variations is drastically reduced, increasing the overall system's reliability and reducing the ordinary and extraordinary maintenance required. Furthermore, WPT represents the best charging technique for autonomous EVs, since the charging process can be completely automated [1].

The structure of a WPT system for EV charging can be divided into three main parts, as shown in Figure 1:

- Primary inverter: generates the alternating voltage waveform used to create the magnetic coupling between the coils.
- Resonant tank: includes the coils and the resonant compensation networks.
- Secondary rectifier: rectifies the coil-induced voltage on the secondary side and controls the output current/voltage to provide the desired charging profile to the vehicle battery.

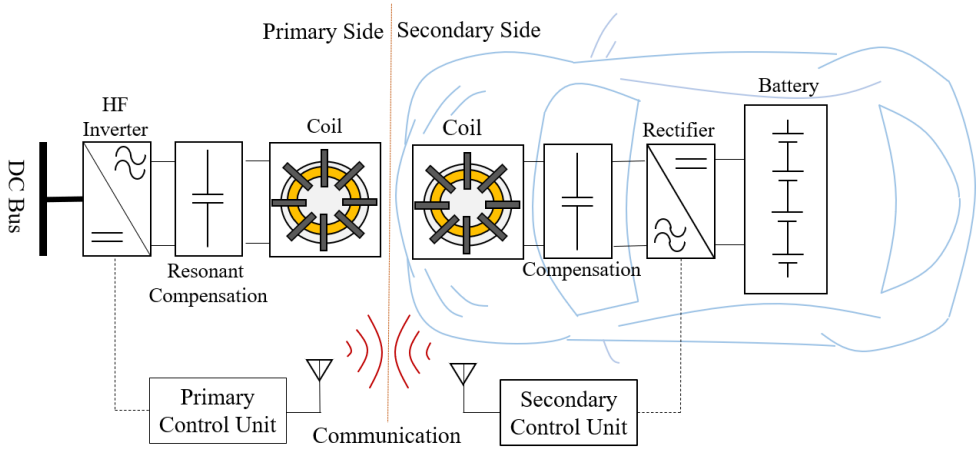

Figure 1. Block scheme of a wireless charging system.

The large air gap between coils leads to operation with low coupling coefficients [2–4]. For this reason, compensation networks are usually used to increase the power and transmission efficiency. These networks are circuits made up from inductors and capacitors tuned to resonate at a specific frequency; when the compensation operates at the resonance frequency, the reactive power is reduced, with a consequent increment in the transmission efficiency. The rapid diffusion of this charging technique leads to the technical standard SAE J2954 [5], which concerns the wireless power transfer for light-duty plug-in/electric vehicles and gives guidelines to encourage compatibility among EV WPT systems. The operating frequency range for EV charging indicated in this standard is (81.39–90) kHz. Although this is a narrow frequency range, a small mismatch between the primary and secondary resonance frequency can also compromise the whole system's performance, due to the high-quality factor of the compensation networks. Thus, the two sides must be optimally tuned to maximize the efficiency and transmitted power.

A communication channel is usually used to share the information between the two sides, as shown in Figure 1. Each channel can provide its operating characteristics to the other and then regulate the operating frequency or the LC compensation component values to operate in optimal conditions. A change in the operating frequency needs a new calibration of the compensation on the new frequency. If only the operating frequency is changed, maintaining the same resonance compensation, the power and transmission efficiency are not maximized [6]. Hence, the primary and secondary side control circuits can adapt their compensation networks to operate at a common operating frequency. This is usually performed through a programmable matrix capacitor or variable inductor [7,8].

The communication channel for the resonance calibration increases the cost and the complexity of the system. Moreover, correct operation is strictly related to its proper operation: if an error occurs during the communication, the system performance is compromised, and this constitutes a critical obstacle to the system's reliability. Furthermore, the coils of these systems are operated at high magnetic fields, which can interfere with data communication [9]. Even if this solution exhibits these disadvantages, the adoption of a communication channel represents the most used solution when the charging process is controlled by the primary inverter. In these systems, usually referred to as primary side controlled systems (PSCS), the secondary side is usually a passive rectifier and the communication channel is used to monitor the state of the battery during the charging process. This solution has already been widely studied in the literature [10–14]; it is hardly suitable for EV charging and requires a communication channel. When the secondary side consists of an active rectifier coordinated with the primary side through a communication channel, the system is called a dual side controlled system (DSCS). These systems have a greater number of degrees of freedom, allow the achievement of high conversion efficiencies, but also entail high costs, and their operating reliability is closely connected to the communication link between the two sides [15,16].

In Figure 2, an overview of EV wireless charging systems is shown. The most widespread architecture is PSCS. It results in high transmission efficiencies (up to $\eta = 96\%$) and the overall system is not excessively complex. The two DSCS systems both exhibit high conversion efficiency (higher than 90%) but the overall system has a larger complexity. Finally, the proposed system is the first secondary side controlled system (SSCS) prototype available in the literature and it is designed to charge an EV battery with $P_o = 3.7$ kW power rating at a DC-DC maximum efficiency of $\eta = 90\%$.

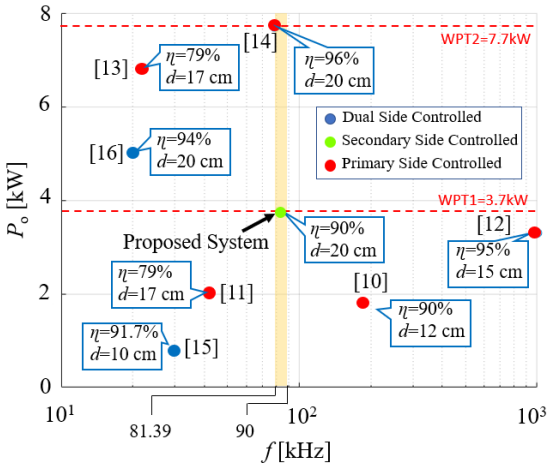

Figure 2. Available wireless charging systems in the literature and their classification according to their control strategy.

In this paper, a novel approach to charging the EV with high transmission efficiency without the use of a communication channel and using a secondary side controlled system is proposed. The on-board vehicle control strategy estimates the transmission frequency of the primary side and adapts the compensation network to properly operate at this frequency, allowing it to work in resonance. No communication channel is required, increasing the system's reliability and flexibility.

Once the charging station and the vehicle are tuned to operate at the optimum resonance frequency, a proper control strategy for the secondary side rectifier is proposed in order to meet two main objectives:

- Provide an appropriate voltage/current charging profile to the battery.
- Maximize the transmission efficiency between the primary and secondary sides.

As previously mentioned, to increase the transmission efficiency over large air gaps, compensation topologies are used. Thanks to its characteristics [17], the series-series (SS) compensation is used in this paper.

The paper is organized as follows. In Section 2, the behavior of the SS compensation is widely studied under variations of the load R_L, the mutual inductance M, and the operating frequency f. In Section 3, the architecture of the system and the modes of operation of the secondary full active rectifier are presented. The impedance matching used to charge the EV and maximize the transmission efficiency is discussed in Section 4. In Section 5, the hardware test-bench and the obtained experimental results are illustrated. Finally, the conclusions are provided in Section 6.

2. Series-Series Compensation

2.1. Topology Description

The equivalent circuit of a series-series (SS) compensation network is shown in Figure 3. The inductances of the coils used to transfer power wirelessly are L_1 and L_2, respectively. The parasitic resistances of the coils are R_1 and R_2, while the capacitances used to operate in resonance are C_1 and C_2. The secondary side is closed on a load resistance R_L. Note that the circuit is supplied by a sinusoidal voltage generator V_1 with an angular frequency ω.

In practice, the primary circuit is powered by a two-level inverter which impresses a square-wave voltage to the primary resonant tank. To study the circuit behavior, the first harmonic approximation (FHA) is used, assuming that higher-order harmonics are filtered by the resonant circuit.

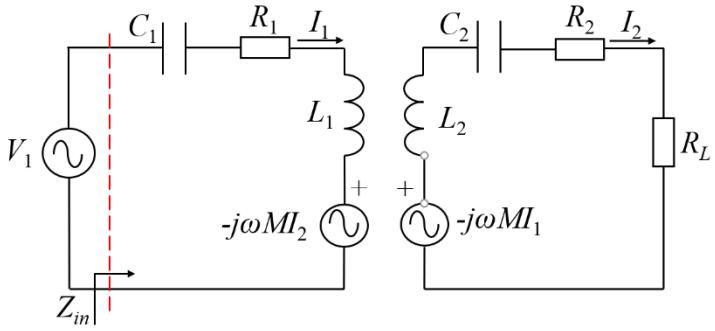

Figure 3. Electric circuit of a series-series compensation.

By using Kirchhoff's voltage laws (KVL), a matrix formulation is extracted [2]

$$\begin{bmatrix} V_1 \\ 0 \end{bmatrix} = \begin{bmatrix} R_1 + j\left(\omega L_1 - \dfrac{1}{\omega C_1}\right) & -j\omega M \\ -j\omega M & R_L + R_2 + j\left(\omega L_2 - \dfrac{1}{\omega C_2}\right) \end{bmatrix} \begin{bmatrix} I_1 \\ I_2 \end{bmatrix} \tag{1}$$

where V_1 is the Root Mean Square (RMS) value of the input voltage; I_1 and I_2 are the primary and secondary current phasor RMS module. By inverting (1), the expressions of the currents on the primary and secondary side are derived as follows:

$$I_1 = \frac{R_2 + R_L + j\left(\omega L_2 - \dfrac{1}{\omega C_2}\right)}{\left[R_1 + j\left(\omega L_1 - \dfrac{1}{\omega C_1}\right)\right]\left[R_2 + R_L + j\left(\omega L_2 - \dfrac{1}{\omega C_2}\right)\right] + \omega^2 M^2} V_1 \tag{2}$$

$$I_2 = \frac{-j\omega M}{\left[R_1 + j\left(\omega L_1 - \dfrac{1}{\omega C_1}\right)\right]\left[R_2 + R_L + j\left(\omega L_2 - \dfrac{1}{\omega C_2}\right)\right] + \omega^2 M^2} V_1 \tag{3}$$

The equivalent impedance $Z_{in} = R_{in} + jX_{in}$ seen from the voltage generator V_1 is

$$Z_{in} = R_{in} + jX_{in} = R_1 + j\omega L_1 - \frac{j}{\omega C_1} + \frac{M^2\omega^2}{j\omega L_2 - \dfrac{j}{\omega C_2} + R_2 + R_L} \tag{4}$$

To cancel the imaginary part X_{in} at the resonance frequency ω_0 and ensure the maximum efficiency and power transfer, the values of the primary and secondary capacitances must be

$$C_1 = \frac{1}{\omega_0^2 L_1}, \quad C_2 = \frac{1}{\omega_0^2 L_2} \tag{5}$$

The transmission efficiency is expressed as

$$\eta = \frac{R_L}{R_L + R_2 + \dfrac{R_1}{\omega^2 M^2}\left[\left(\omega L_2 - \dfrac{1}{\omega C_2}\right)^2 + \left(R_2 + R_L\right)^2\right]} \tag{6}$$

If the system is operated under resonance condition—that is, $\omega = \omega_0$, and the capacitances C_1 and C_2 are tuned according to (5)—(6) simplifies as

$$\eta = \frac{R_L}{R_L + R_2 + \frac{R_1}{\omega^2 M^2}\left(R_2 + R_L\right)^2} \tag{7}$$

and the power transferred to the load is

$$P_o = R_L I_2^2 = R_L \left(\frac{V_1 \omega M}{R_1\left(R_2 + R_L\right) + \omega^2 M^2} \right)^2 \tag{8}$$

Note that if the parasitic resistances R_1 and R_2 are neglected, the output power is $P_o = R_L V_i^2/(\omega_0 M)^2$. Thus, the SS compensation acts approximately as the current source, and the output power increases as the load resistance R_L increases.

2.2. Mutual Inductance Sensitivity Analysis

By computing the derivative of the efficiency expression, it is possible to study how it is affected by the mutual inductance.

$$\frac{\partial \eta}{\partial M} = \frac{2 M R_1 R_L \omega^2 \left(R_2 + R_L\right)^2}{\left\{\left[\left(R_2 + R_L\right)\omega^2 M^2\right] + \left[R_1\left(R_2 + R_L\right)^2\right]\right\}^2} \tag{9}$$

The derivate is always positive: the efficiency increases as the mutual inductance increases. To reach high transmission efficiency, high coupling between coils is needed. The same approach is used to exploit the dependence of the output power on the mutual inductance. From (8), the output power P_o is maximized when the secondary current I_2 is maximized with respect to M; thus,

$$\frac{\partial I_2}{\partial M} = \frac{V_1 \omega R_1\left(R_2 + R_L\right) - V_1 \omega^3 M^2}{\left\{\left[R_1\left(R_2 + R_L\right)\right] + \omega^2 M^2\right\}^2} \tag{10}$$

From (10), the value of mutual inductance which maximizes the transmission efficiency is derived as

$$M^{P_o} = \sqrt{\frac{R_1\left(R_2 + R_L\right)}{\omega^2}} \tag{11}$$

2.3. Operating Frequency Sensitivity Analysis

According to (6), the expression of the efficiency is rearranged as follows:

$$\eta(\omega) = \frac{N(\omega)}{D(\omega)} = \frac{\omega^4 C_2^2 M^2 R_L}{\omega^4 C_2^2\left[M^2 R + L_2^2 R_1\right] + \omega^2 R_1\left[C_2^2 R^2 - 2 L_2 C_2\right] + R_1} \tag{12}$$

To understand the value of ω which maximizes the efficiency, its derivative is studied; hence,

$$\frac{\partial \eta(\omega)}{\partial \omega} = \frac{N'(\omega) D(\omega) - N(\omega) D'(\omega)}{D^2(\omega)} = \frac{2\omega^3 C_2^2 M^2 R_1 R_L\left[\omega^2\left[C_2^2 R^2 - 2 L_2 C_2\right] + 2\right]}{D^2(\omega)} \tag{13}$$

Assuming the secondary capacitance C_2 designed to resonate with the secondary inductance L_2 at the resonant frequency ω_0, the angular frequency ω^{η} which maximizes the efficiency is

$$\omega^{\eta_{\max}} = \sqrt{\frac{1}{\frac{1}{\omega_0^2} - \frac{1}{2} R^2 C_2^2}} \tag{14}$$

Being $\frac{1}{\omega_0^2} \gg \frac{1}{2}R^2C_2^2$, (14) simplifies to

$$\omega^{\eta_{\max}} = \omega_0 = \frac{1}{\sqrt{L_2C_2}} \tag{15}$$

This confirms that the main advantage of operating at the resonance is the transmission efficiency maximization. Deriving (8) with respect to ω, the angular frequency which maximizes the output power is

$$\omega^{P_o} = \sqrt{\frac{R_1(R_2+R_L)}{M^2}} \tag{16}$$

2.4. Load Resistance Sensitivity Analysis

Defining $\delta = M^2R_2 + L_2^2R_1$ and $\psi = C_2R_2^2 - 2L_2$, the expression of the efficiency as a function of the load resistance is as follows:

$$\eta(R_L) = \frac{\omega^2M^2C_2^2R_L}{C_2^2R_1R_L + C_2^2\left[\omega^2M^2 + 2R_1R_2\right]R_L + \omega^2C_2^2\delta + C_2R_1\psi + \frac{R_1}{\omega^2}} \tag{17}$$

Deriving (17) respect to R_L, we obtain

$$\frac{\partial\eta}{\partial R_L} = \frac{\omega^4M^2C_2^4\delta + \omega^2M^2C_2^3R_1\psi + M^2C_2^2R_1}{D^2(R_L)} \tag{18}$$

Studying (18), the load resistance which maximizes the transmission efficiency is derived as

$$R_L^\eta = \sqrt{\frac{\omega^4C_2^2\left[M^2R_2 + L_2^2R_1\right] + \omega^2C_2R_1\left[C_2R_2^2 - 2L_2\right] + R_1}{\omega^2C_2^2R_1}} \tag{19}$$

If the system works at the resonant frequency $\omega = \omega_0$ and the capacitances C_1 and C_2 are designed according to (5), (19) simplifies as follows:

$$R_L^\eta = R_2\sqrt{1 + \frac{\omega^2M^2}{R_1R_2}} \tag{20}$$

The results of the previous analysis are summarized in Table 1.

Table 1. Series-series compensation optimal parameter.

Parameter	Value Which Maximizes η	Value Which Maximizes P_o
R_L	$R_L^\eta = R_2\sqrt{1 + \frac{\omega^2M^2}{R_1R_2}}$	$\uparrow P_o$
M	$\uparrow \eta$	$M^{P_o} = \sqrt{\frac{R_1(R_2+R_L)}{\omega^2}}$
ω	$\omega^\eta = \sqrt{\frac{1}{L_2C_2}}$	$\omega^{P_o} = \sqrt{\frac{R_1(R_2+R_L)}{M^2}}$

The following design considerations must be satisfied to reach a high transmission efficiency:

- Equation (14) indicates that the maximum efficiency is reached when the system operates in resonance. The capacitances C_1 and C_2 must be maintained constantly tuned with the operating frequency according to (5). In practice, in an SSC system, the primary capacitance is fixed and

tuned to operate at the resonance frequency ω_0, while the secondary capacitance C_2 is changed and tuned to resonate at ω_0.

- Equation (9) shows that efficiency increases as the mutual inductance increases. Attention must be placed on the coil geometry design to reach high coupling.
- The efficiency is maximized for a particular value of equivalent impedance $R_L{}^{\eta}$, as shown by (19). The proposed control strategy allows charging of the the EV battery operating at $Z_{eq} = R_L{}^{\eta}$ during the whole charging process.

3. WPT Control Strategy

In this section, the control strategy used to regulate the secondary side is presented. The circuit of the proposed wireless charging system is shown in Figure 4.

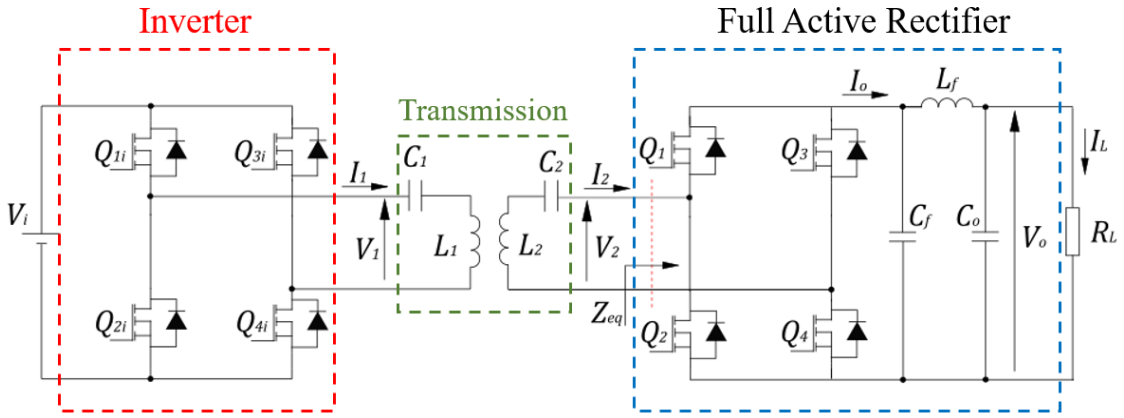

Figure 4. The secondary side-controlled system with a series-series compensation circuit.

The system is supplied with a DC voltage V_i. The full-bridge inverter circuit at the primary stage generates a square-wave voltage V_s at a frequency f_0 with amplitude $\pm V_i$. The voltage waveform is delivered to the primary side resonant tank and, then, to the wireless link. As described in the previous section, the capacitors C_1 and C_2 are tuned to resonate with the transmission coil inductances L_1 and L_2. Then, the sinusoidal current transmitted on the secondary side I_2 is rectified through a full active rectifier (FAR) composed of four MOSFETs, Q_1, Q_2, Q_3, and Q_4. To perform the analysis of the system, the first harmonic analysis (FHA) is used, taking into account only the first harmonic of the square voltage V_s and neglecting the higher-order harmonics. Hence, only the RMS value V_1 of the first harmonic of the voltage V_S is taken into account. The DC current I_o at the output of the FAR goes through a CLC low-pass filter and, then, it is used to supply the EV battery. By properly switching the FAR MOSFETs, the average value of the output current I_o is regulated and, therefore, the current delivered to the load resistance R_L is also regulated.

The FAR control strategy is based on duty-cycle and phase shift variations [15]. This section aims to explain the states of operation of the control strategy and derive the analytical expression of the equivalent impedance as a function of the duty cycle β and phase shift φ. The modes of operation of this technique are shown in Figure 5.

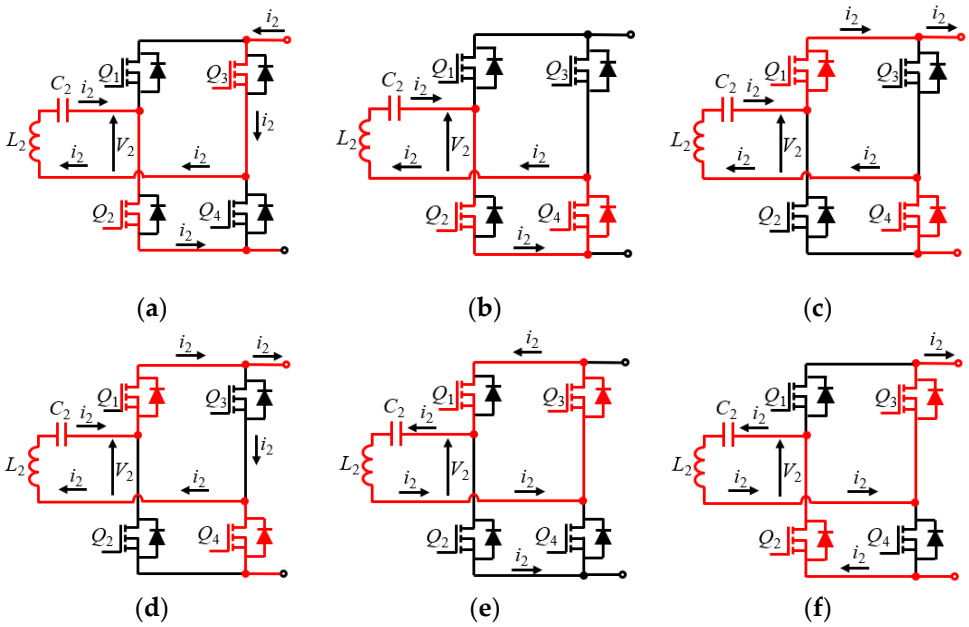

Figure 5. Modes of operation of the full active rectifier. (**a**) State A. (**b**) State B. (**c**) State C. (**d**) State D. (**e**) State E. (**f**) State F.

If the voltage V_s lags behind the current I_2, as shown in Figure 6a, the states of operation are [15]:

- State A ($0 < \omega t < \omega t_0$): During this interval, both the MOSFETs Q_2 and Q_3 are turned ON. In this state, the current flows from the capacitance load to the rectifier circuit. By hard switching (Turn Off) Q_3 and soft switching (Turn On) Q_4, the control switches to the following state.
- State B ($\omega t_0 < \omega t < \omega t_1$): The voltage V_2 is shorted to ground through Q_2 and Q_4. No power is transferred to the load. By hard switching Q_2 and soft switching Q_1, the control switches to the following state.
- State C ($\omega t_1 < \omega t < \omega t_2$): The current flows through the load and power is transferred. No action is taken.
- State D ($\omega t_2 < \omega t < \omega t_3$): The current flows in the opposite direction with respect to State C. As in State A, the power is extracted from the load to the circuit. By turning off Q_4 and turning on Q_3, the control switches to the next state.
- State E ($\omega t_3 < \omega t < \omega t_4$): The resonant tank is short-circuited, and no power is delivered to the load. By turning on Q_2 (soft switching) and turning off Q_1, the control switches to the next state.
- State F ($\omega t_4 < \omega t < \omega t_5$): The current flows to the load until it changes the polarity and State A occurs again.

By defining β, the duration of the pulse of the input rectifier, and φ, the phase shift between the fundamental component of V_s and of the current I_2, three different modes of operation can be identified. If the shift angle $\varphi < 0$, the equivalent impedance of the FAR is capacitive-resistive. If $\varphi = 0$, the impedance Z_{eq} is purely resistive; if $\varphi > 0$, the impedance Z_{eq} is inductive-resistive.

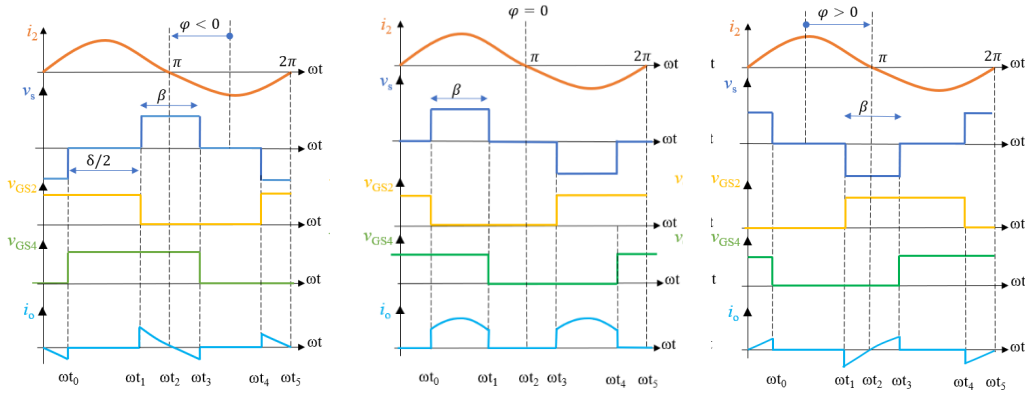

Figure 6. Modes of operation. (**a**) Case with phase shift angle $\varphi < 0$. (**b**) Case with phase shift angle $\varphi = 0$. (**c**) Case with phase shift angle $\varphi > 0$.

The voltage V_2 at the input of the rectifier, written as phasor, is

$$\overline{V}_s = \frac{2\sqrt{2}}{\pi} V_o \sin\left(\frac{\beta}{2}\right) e^{j\varphi} \tag{21}$$

According to the waveforms of Figure 6a, the expression of the average of the output current I_o is

$$I_o = \frac{1}{\pi} \int_{\frac{\pi}{2}-\frac{\beta}{2}-\varphi}^{\frac{\pi}{2}+\frac{\beta}{2}-\varphi} i_2(\omega t) d\omega t = \frac{1}{\pi} \int_{\frac{\pi}{2}-\frac{\beta}{2}-\varphi}^{\frac{\pi}{2}+\frac{\beta}{2}-\varphi} I_2^{\max} \sin(\omega t) d\omega t = \frac{2\sqrt{2}}{\pi} I_2^{rms} \sin\left(\frac{\beta}{2}\right) \cos\varphi \tag{22}$$

The equivalent impedance of the rectifier is expressed as

$$Z_{eq} = \frac{V_s}{I_2^{rms}} = \frac{8}{\pi^2} R_L \sin\left(\frac{\beta}{2}\right) \cos(\varphi) e^{j\varphi} = \frac{4}{\pi^2} R_L (1 - \cos\beta) \cos(\varphi) e^{j\varphi} \tag{23}$$

The real and imaginary parts of the impedance are

$$R_{eq} = \frac{4}{\pi^2} R_L (1 - \cos\beta) \cos^2(\varphi) \tag{24}$$

$$X_{eq} = \frac{4}{\pi^2} R_L \sin(\varphi) \cos(\varphi) (1 - \cos\beta) \tag{25}$$

respectively. Imposing the optimum condition $R_{eq} = R_L^{\eta}$ and solving (25) and (26), one obtains

$$\varphi = arctg\left(\frac{X_{eq}}{R_L^{\eta}}\right) \tag{26}$$

$$\beta = \arccos\left(1 - \frac{\pi^2 R_L^{\eta}}{4 R_L \cos^2(\varphi)}\right) \tag{27}$$

From (27), the condition under which it is possible to operate with $R_{eq} = R_L^{\eta}$ is

$$\frac{R_L^{\eta}}{R_L} < \frac{8}{\pi^2} \cos^2(\varphi) \tag{28}$$

As shown in (24), being the resistive part of the equivalent impedance dependent on both φ and β, multiple combinations (φ, β) can satisfy the condition $R_{eq} = R_L^{\eta}$. Using (27), the set of solutions (φ, β) which satisfy the condition $R_{eq} = R_L^{\eta}$ for different values of the load resistance R_L is shown in Figure 7. The condition (27) is in line with the plot trends of Figure 7; it is possible to notice that the phase span of the angle φ decreases by increasing the ratio R_L^{η}/R_L. Thus, there is a set of solutions (φ, β) that make it possible to operate within the condition $R_{eq} = R_L^{\eta}$. The reactive part of the rectifier X_{eq} is equal to zero when $\varphi = 0$. The efficiency is maximized when the resonant tank is connected to a purely resistive load R_L^{η} and thus a phase shift angle of $\varphi = 0$ is chosen.

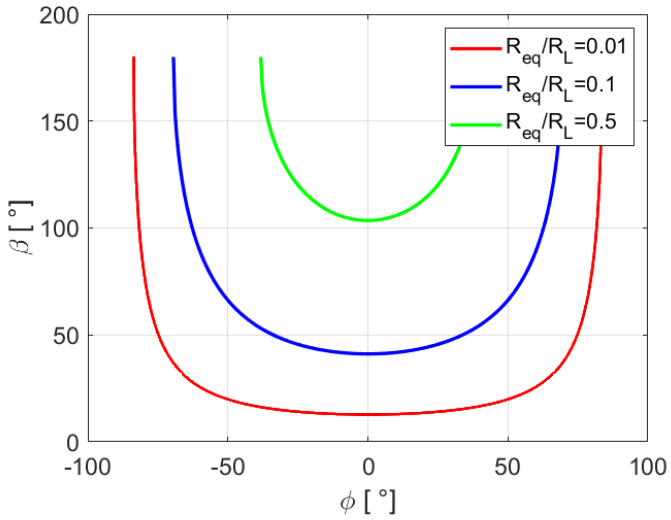

Figure 7. Solution set (φ, β) resulting in an operation with $R_{eq} = R_L^{\eta}$.

4. Impedance Matching

In the previous section, the possibility to reach the condition $R_{eq} = R^{\eta}$ has been demonstrated. As shown in Section 2, the achievement of this condition leads the circuit to operate at a maximum transmission efficiency. In any case, EV charging also requires the battery to be supplied with a proper current/voltage profile. For this reason, in this section, a control strategy able to perform these two operations simultaneously through impedance matching is presented.

To provide a current to the load I_o^{ref} and simultaneously maximize the transmission efficiency, the following conditions are required:

$$\begin{cases} I_o = I_o^{ref} = \dfrac{2\sqrt{2}}{\pi} I_2 \sin\left(\dfrac{\beta}{2}\right)\cos\varphi \\ R_{Leq} = R_L^{\eta} = \dfrac{4}{\pi^2} R_L \cos^2(\varphi)\left[1-\cos(\beta)\right] \end{cases} \tag{29}$$

The first equation of the system can be written as

$$\cos\varphi = \frac{\pi I_o^{ref}}{2\sqrt{2} I_2 \sin\left(\dfrac{\beta}{2}\right)} \tag{30}$$

Managing the system of Equation (29), the following relationship is obtained:

$$\frac{1-\cos\beta}{\sin^2\left(\dfrac{\beta}{2}\right)} = 2\frac{R_L^{\eta}}{R_L}\left(\frac{I_2}{I_o}\right)^2 \tag{31}$$

which indicates that the control angle β must be changed according to the current induced on the secondary coil I_2 and the desired output current I_o.

By imposing $sin\left(\frac{\beta}{2}\right) = \sqrt{\frac{1-cos\beta}{2}}$, (31) simplifies as follows:

$$1 = \frac{R_L^{\eta}}{R_L}\left(\frac{I_2}{I_o^{ref}}\right)^2 \tag{32}$$

Using (32) and the second equation of (29), and assuming to operate at $\varphi = 0$, the following condition is obtained:

$$\cos\beta = 1 - \frac{\pi^2}{4} R_L^{\eta}\left(\frac{I_o}{I_2}\right)^2 \tag{33}$$

which can also be written as

$$\frac{R_L^{\eta}}{R_L} = \left(\frac{I_o^{ref}}{I_2}\right)^2 \Rightarrow \frac{R_L^{\eta}}{V_o I_o^{ref}} = \frac{1}{I_2^2} \quad (34)$$

Therefore, the condition needed to deliver the desired output current I_o^{ref} and simultaneously operate at the highest transmission efficiency is

$$P_o = V_o I_o^{ref} = R_L^{\eta} I_2^2 \quad (35)$$

Note that this condition represents the conservation of energy. Assuming that the FAR has efficiency 1, the input power is equal to the output power. For static charging applications, the resistance which maximizes the transmission efficiency R_L^{η} can be assumed constant. As shown by (20), it depends on the mutual inductance M, the parasitic resistances of the coils R_1 and R_2, and the angular frequency ω, which are assumed to be constant in this project. The control of the proposed system being placed on the secondary side, also the primary voltage V_1 can be assumed to be constant. Thus, as shown in (8), also the secondary current I_2 can be assumed constant and approximately independent from the load R_{eq}. Therefore, there are two substantial consequences of (35):

- Usually, the EV is charged with the constant current/constant voltage profile (CC/CV). As shown in Figure 8a, in this case, the current is maintained constant until the voltage reaches a threshold value V_{th}. Thus, using CC/CV, the system must be thermally designed to operate at P_{max}, even if the system operates in this condition only for a short time. Thus, the system is thermally oversized during most of the charging process. By using CP charging, the power is constant until the state of charge of the battery is 100%, as shown in Figure 8b, and, therefore, the system can be thermally designed to operate at P_{max}, which corresponds to the power during the whole charging process. As a result, oversizing is avoided and both weight and cost reduced. As shown in (35), the proposed system has to maintain the power constant during the whole process to maximize transmission efficiency.
- The value of the power charging P_o is dependent on R_L^{η}; thus, to transfer a specific rated power, attention must be placed on the coil pad layout. Assuming to operate at a fixed angular frequency ω and assuming that the DC primary voltage V_i is constant, the value of the transferred power depends on the value of mutual inductance M and on the primary and secondary parasitic resistances R_1 and R_2. Thus, a proper geometric design of the coil must be performed to achieve the desired output power.

In the next section, the design procedure used to design a P_o = 3.7 kW charging system is presented.

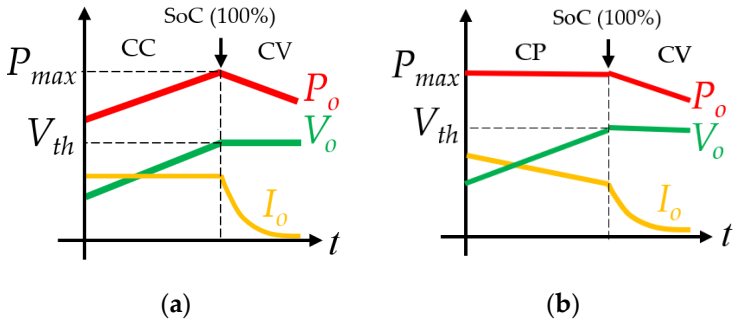

Figure 8. Different charging profiles. The red lines represent the power delivered to the EV battery, the green line is the EV battery voltage, and the yellow line represents the current. (**a**) Constant current/constant voltage charging profile. (b) Constant power charging profile.

4.1. Coil Design for Maximum Efficiency Transmission

As mentioned in the previous section, this paper aims to design an EV system able to charge a battery with P_o = 3.7 kW, ensuring the maximum transmission efficiency η_{max} during the whole charging process. From (7) and (8), the analytical expression of the output power and transmission efficiency are evaluated. These two parameters are highly dependent on the mutual inductance M

and the parasitic resistances R_1 and R_2. Thus, the performance of the whole system is highly dependent on the design of the coils. In this section, the threshold value of mutual inductance M_{min} and the maximum values of parasitic resistances R_1^{max} and R_2^{max} needed to charge the battery at a desired power rate P_o with a maximum transmission efficiency η_{max} are derived. It is assumed that the primary and secondary coils have the same geometry and, then, $R_1 = R_2 = R$. Operation at P_o and η_{max} can be mathematically written as

$$P_o = R_L^{\eta} I_2^2 = \frac{\alpha\omega^2 M^2 R V_1^2}{R^4(1+\alpha)^2 + 2\omega^2 M^2 R^2(1+\alpha) + \omega^4 M^4} = \frac{\alpha\omega^2 M^2 R V_1^2}{\left[R^2(1+\alpha) + \omega^2 M^2\right]^2} \quad (36)$$

where $\alpha = \sqrt{1 + \frac{\omega^2 M^2}{R^2}}$. Defining $f(M,R) = P_o[R^2(1+\alpha) + \omega^2 M^2]^2$ and $g(M,R) = \alpha\omega^2 M^2 R V_1^2$, Equation (36) can be rearranged as

$$f(M,R) = g(M,R) \quad (37)$$

Studying (37), the threshold values of M^{min} and R^{max} which make it possible to transfer P_o with a maximum efficiency η_{max} can be found. The procedure that can be used to identify the characteristics of the coils is summarized in Figure 9.

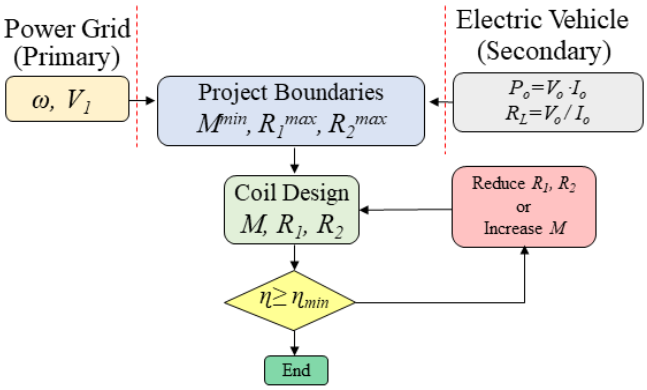

Figure 9. Optimal procedure for transmission circuit sizing.

Firstly, the characteristics of the primary inverter must be defined to extrapolate the operating frequency ω and the first harmonic RMS value V_1 of the square wave impressed to the resonant tank. Then, the EV battery characteristics have been considered to decide the charging power rate P_o.

As shown in Figure 9, an iterative design procedure for the design of the coils is required. Assuming to operate with a threshold value of mutual inductance M^{min}, using (37), the maximum parasitic resistances R_1^{max} and R_2^{max} which allow operation at the maximum efficiency η_{max} during the whole charging process are calculated.

Therefore, once the coil geometry is defined, it is sufficient to verify $M > M^{min}$ and also $R_1 < R_1^{max}$ and $R_2 < R_2^{max}$. If these conditions are satisfied, the proposed technique can be implemented and the circuit operates at the maximum efficiency; otherwise, it is necessary to modify the coil geometry to operate within the limits.

In the proposed secondary side-controlled system, the frequency and the voltage at the output of the primary inverter can be assumed constant and equal to $f = 85$ kHz and $V_1 = 293$ V, respectively. The output power is fixed to $P_o = 3.7$ kW. These characteristics are summarized in Table 2.

Table 2. WPT setup parameters.

Parameter	Value	Description
f_0	85 kHz	Operating Switching Frequency
V_1	293 V	1st Harmonic RMS Value of the Inverter Square Waveform
P_o	3.7 kW	Output Power

The functions $f(M, R)$ and $g(M, R)$ are represented for three different values of mutual inductance in Figure 10, using the values shown in Table 2.

Assuming a mutual inductance M_{min} = 20 μH, the maximum allowed values for parasitic resistances are $R_{1max} = R_{2max}$ = 0.78 Ω. If the minimum mutual inductance is lower, e.g., M_{min} = 15 μH, the maximum parasitic resistances must be $R_{1max} = R_{2max}$ = 0.61 Ω. Finally, if the magnetic coupling is M_{min} = 10 μH, the maximum parasitic resistance values are $R_{1max} = R_{2max}$ = 0.43 Ω. As a result, the lower is the coupling among the coils, the lower must be the coil parasitic resistances.

Following the guidelines presented [18] concerning the design of the copper coils, ferrite bars, and aluminum shielding, a pad able to satisfy (37) has been created. The coils are represented in Figure 11a. The primary side coil has an inductance L_1 = 89.22 μH and parasitic resistance R_1 = 0.055 Ω. The secondary side coil has an inductance of L_2 = 90.02 μH and parasitic resistance R_2 = 0.061 Ω. The measured mutual inductance over the distance between the coils is shown in Figure 11b. It can be seen that at a distance d = 20cm, the mutual inductance is M = 15.8 μH. Using (37), the maximum parasitic resistances which allow operation at the maximum efficiency are $R_1^{max} = R_2^{max}$ = 0.63 Ω. Being $R_1 < R_1^{max}$ and $R_2 < R_2^{max}$, the maximum efficiency can be maintained during the whole charging process.

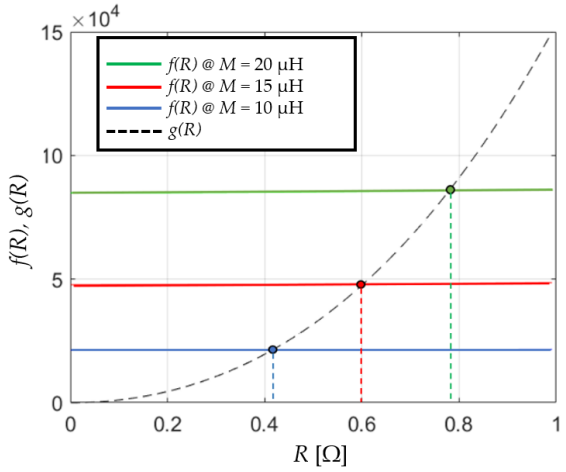

Figure 10. Graphical representation of (38). The trend of the function f is nearly linear in the range $0 < R < 1$.

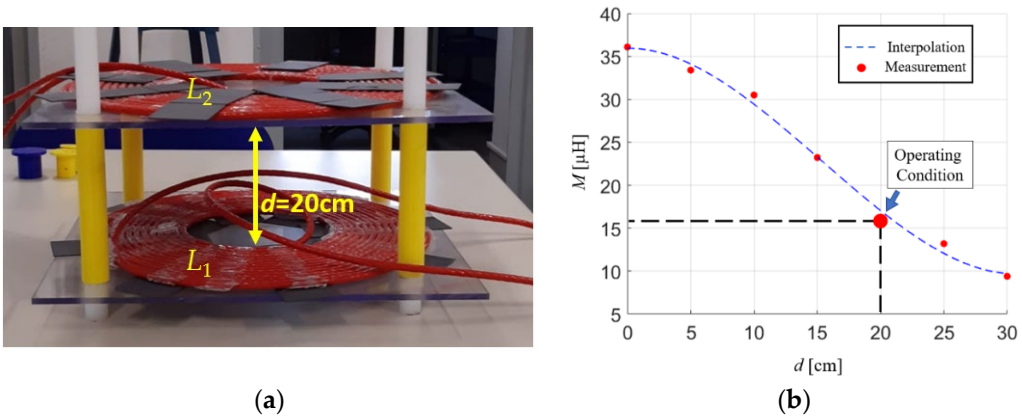

(**a**) (**b**)

Figure 11. Wireless power transfer coils. (**a**) Pictures of the coils. (**b**) Measured mutual inductance as a function of pad distance.

The characteristics of the transmitter and receiver coils are summarized in Table 3.

Table 3. WPT setup parameters.

Parameter	Value	Description
d	20 cm	Distance between Primary and Secondary Coils
M	15.8 μH	Mutual Inductance
L_1	89.22 μH	Primary Coil Inductance
R_1	55 mΩ	Primary Coil Parasitic Resistance
L_2	90.02 μH	Secondary Coil Inductance
R_2	61 mΩ	Secondary Coil Parasitic Resistance

4.2. Capacitor Matrix Design

Particular attention has been paid to the secondary resonant capacitor. As stated before, to guarantee compatibility between the primary and the secondary side, the capacitance C_2 is tuned to resonate with the secondary coil L_2 at the primary resonant frequency, which is in the (81.39–90) kHz range, as stated by the SAE J2954 standard. The choice of the capacitor heavily affects the performance of the entire system for the following reasons:

- The capacitors are crossed by high currents (up to 70 A) at high frequencies (SAE range); therefore, high parasitic resistances can lead to high power losses, with the consequent reduction in the transmission efficiency and rise in thermal dissipation issues.
- The value of the capacitance must be stable and accurately tuned with respect to the secondary coil and operating frequency, as shown in (5), because it is used to create a resonance between the primary and the secondary side and any variations drastically reduce the system's performance.

For this reason, to allow resonance throughout the frequency range indicated by the SAE standard and at the same time ensure low parasitic resistances, a programmable matrix architecture was selected.

This solution allows the variation of the equivalent capacitance value by adding or removing capacitors from the matrix and, at the same time, the distribution of the currents and voltages on the capacitors so that the stresses on each component are reduced.

The RMS value of the current through the matrix capacitor is approximately $I_2 = V_i/(\omega M) \cong 65$ A. Being $L_2 = 90$ μH, using (5), the value of the capacitance which allows operation in resonance is $C_2 = 38.95$ nF. Thus, the RMS value of the voltage across the matrix capacitor is $V_{C2} \cong 3124.3$ V.

The utilized capacitor is an SNFP X0 2330 7D 4A KS00 from WIMA (Germany). Each capacitor has a nominal value $C = 33$ nF and sustains a rated 4000 V DC voltage. The maximum voltage at which the capacitor is operated decreases when the frequency increases. For this capacitor, at $f = 100$ kHz, the maximum voltage is approximately $V_C^{max} = 300$ V, while the current $I_C^{max} = 7$ A.

Thus, to safely distribute the current in each capacitor of the matrix, the minimum number of capacitors to be connected in parallel is $N_{parallel}^{min} = I_2/I_C^{max} \cong 9$, while, to distribute the overall voltage, the number of capacitors to be connected in series is $N_{series}^{min} = V_{C2}/V_C^{max} = 11$.

As a result, the adopted matrix is composed of strings constituted by $N_{series} = 12$ capacitors connected in series, while $N_{parallel}$ can be changed to maintain the system in resonance, as shown in Figure 12. Here, the blue line represents the value of C_2 calculated using (5) at different frequencies. To operate as closely as possible to the resonance, the matrix of capacitors is adjusted by adding or removing the number of strings in parallel according to the primary operating frequency. This task is easily achieved by using a switching MOSFET which is turned on to add additional parallel strings. Note that the requirement in terms of MOSFET breakdown voltage and continuous current is not critical, as the flowing current is limited to $I_2/N_{parallel} \cong 5$ A, and the voltage is $V_{C2}/N_{series} = 284$ V. Moreover, only two MOSFETS are required in a $N_{series} = 12$ and $N_{parallel} = 13$ capacitor matrix to guarantee the resonance in the SAE J2954 frequency range.

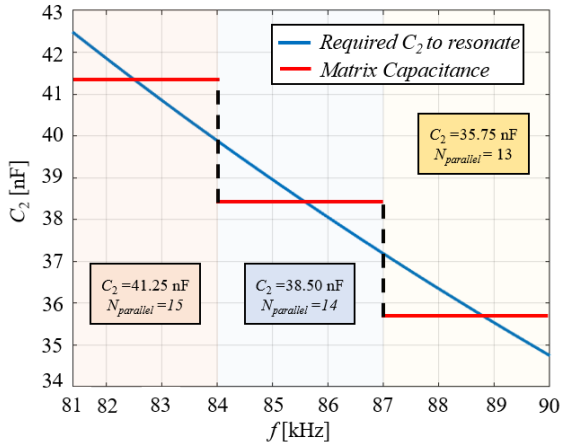

Figure 12. Matrix capacitance for different values of operating frequencies.

5. Test Bench and Experimental Results

In this section, the architecture of the proposed system is described. The electric circuit of the secondary full active rectifier is shown in Figure 13. Each switching cell is a SCT3022AL SiC MOSFET by Rhom Semiconductor (Japan) and a 1EDC60H12AH MOSFET driver by Infineon (Germany). To perform the control strategy, both the current flowing in the secondary coil i_2 and the current delivered to the battery I_o must be measured. The secondary coil current i_2 is measured through two shunt resistors placed as shown in Figure 13. The current measurement is simplified because one side of the shunt resistor is referred and also the common mode requirements of the ICs are reduced.

The current delivered to the battery I_o has a low dynamic; thus, an ACS770KCB-050-PFF-T Hall sensor by Allegro (USA) is used. The red lines in the schematic represent the measurements of the current, which are processed by the Nucleo STM32H743ZIT6 control board by ST (Italy). The power boards used are the same for both the primary inverter and secondary rectifier and are shown in Figure 14, while the whole system setup is shown in Figure 15.

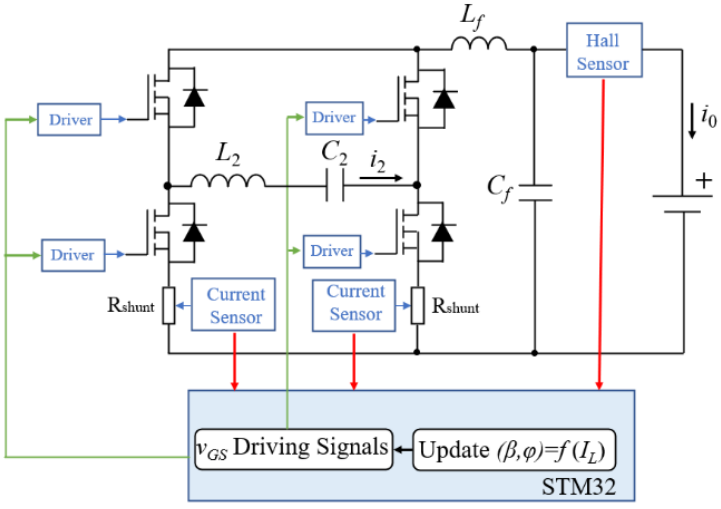

Figure 13. The control scheme and current measurement of the secondary rectifier.

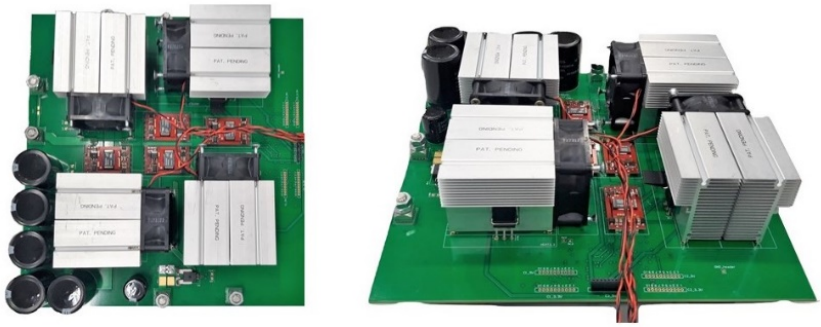

Figure 14. Power boards used for both the primary inverter and secondary rectifier.

The measured current and voltage waveforms at the input of the active rectifier for different values of control angles φ and β are shown in Figure 16. In Figure 16a the voltage v_2 and the current i_2 operating with $\varphi = 0$ and $\beta = \pi/2$ are shown. In Figure 16b the case with $\varphi = \pi/8$ and $\beta = \pi/4$ is show while in Figure 16c the case with $\varphi = -\pi/8$ and $\beta = \pi/4$.

From these waveforms, it can be seen that the output power is regulated through the control angle β. Increasing this angle, the value of the averaged current transferred to the load increases, boosting the output power. The amplitude of the voltage V_2 corresponds to the output voltage. Thus, as expected, it can be seen that the output voltage is lower for $\beta = \pi/4$ than $\beta = \pi/2$.

The system efficiency is plotted in Figure 17a at different output power values. To produce an equivalent impedance $Z_{eq} = R_L{}^n$, the active rectifier operates with $\varphi = 0$ and regulates the value of β according to the value of the measured secondary current I_2 and that of the output current I_o as given in (22). The green trace in Figure 17a represents the maximum transmission efficiency achieved when the active rectifier operates with $Z_{eq} = R_L{}^n$. This limit does not take into account the power losses due to parasitic components and switching losses.

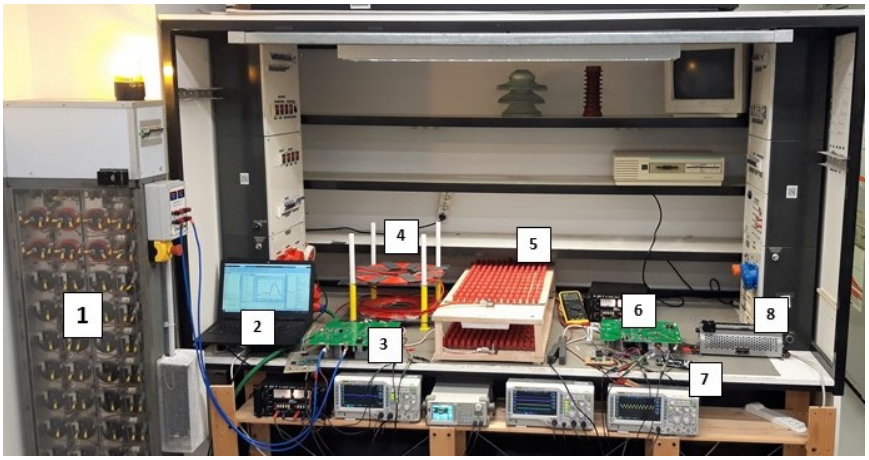

Figure 15. WPT experimental setup. 1: Three-phase rectifier. 2: PC for measurement analysis. 3: Primary inverter. 4: Coil inductances. 5: Resonant capacitances. 6: Active rectifier. 7: STM control board. 8: Load resistance.

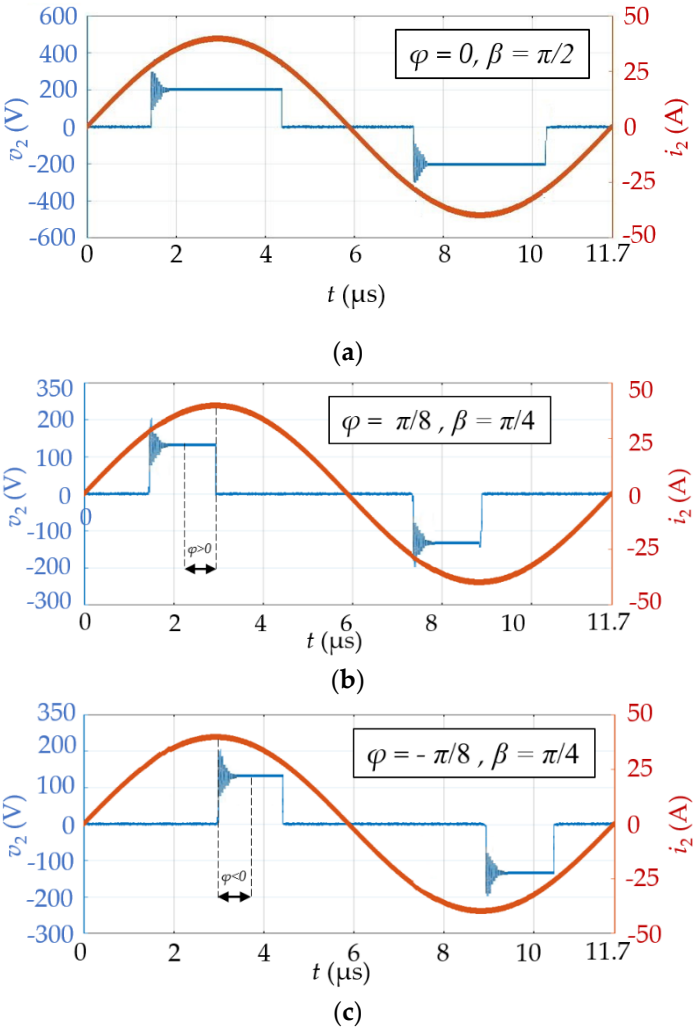

Figure 16. Measured voltage and current waveforms at the input of the FAR with load resistance R_L = 10 Ω. (**a**) Test with $\beta = \pi/2$ and $\varphi = 0$. (**b**) Test with $\beta = \pi/4$ and $\varphi = \pi/8$. (**c**) Test with $\beta = -\pi/4$ and $\varphi = \pi/8$.

The performance of the system has been evaluated for different values of output power and output current ratings. Figure 17 shows that DC-DC efficiency increases as the transferred power increases. For higher output currents, the efficiency of the system decreases.

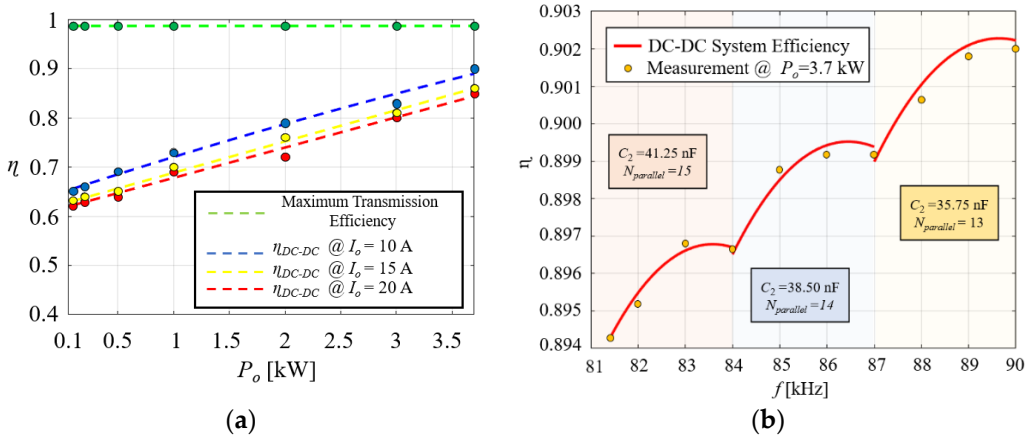

Figure 17. System efficiency. (**a**) DC-DC efficiency comparison at different values of output current I_o and for different output power P_o values. (**b**) DC-DC efficiency obtained through the programmable matrix capacitance for different values of operating frequency.

Finally, to validate the performance of the proposed system to operate with a primary side independently of its resonant frequency, the efficiency of the system over the entire SAE J2054 frequency range has been evaluated at a constant output power P_o = 3.7 kW.

The efficiency as a function of frequency is plotted in Figure 17b, which clearly shows the capability of the programmable capacitor matrix to regulate the secondary compensation and operate at the highest efficiency for a given primary operating frequency.

6. Conclusions

In this paper, the analysis, design, and experimental tests of a secondary side controlled wireless charging system are presented. Unlike most of the wireless charging systems available in the literature, the charging process is completely managed from the vehicle side.

The main novel contributions of the paper are as follows:

- Compatibility between primary and secondary side: the on-board vehicle capacitance C_2 is tuned to resonate with the secondary coil L_2 at the primary resonant frequency, which is in the range (81.39–90) kHz, as stated in the SAE J2954 standard. This innovative solution allows for adapting the characteristics of the secondary circuit to the primary characteristics, making it possible to charge the vehicle independently of the primary. Moreover, thanks to this operation, the primary and secondary constantly operate in resonance, ensuring high transmission efficiency.
- The vehicle is charged at the maximum transmission efficiency: the proposed control strategy allows it to operate at the maximum transmission efficiency over the entire charge process by operating continuous impedance matching; that is, the active rectifier input impedance, as seen by the primary side, is an equivalent impedance Z_{eq} equal to the optimum resistance of the series-series compensation $R_{Lη}$. As a result, the transmission efficiency is constantly maximized. The conditions under which this operation is achieved have been analytically derived and experimentally validated.

A test bench has been built to verify the performance of the proposed system and the experimental results confirmed the ability of the secondary side to adapt the capacitor matrix so that it resonates with the primary.

The system can reach a DC-DC efficiency as high as $\eta_{DC\text{-}DC}$ = 90% at P_o = 3.7 kW. As a future development, coil geometries able to increase the magnetic coupling, reduce the dispersed flux, and increase the transmission efficiency will be investigated.

Zero voltage switching techniques to reduce the switching losses of the MOSFETs and achieve higher conversion efficiencies will be studied.

Author Contributions: Conceptualization, F.C., A.R., A.N., L.P.; methodology, F.C., A.N.; software, L.P., E.G., F.G., M.N.; validation, A.R., A.N.; formal analysis, F.C.,A.R.,A.N.; investigation, F.C., L.P., E.G.; resources, F.C., L.P. L.P. F.G; data curation, F.C., L.P. L.P. F.G; writing—original draft preparation, F.C., A.R. L.P.; writing—review and editing, F.C., A.R., L.P.; supervision, A.R., A.N., M.N., F.G., L.P., M.P.; project administration, A.R., A.N., M.N., F.G., L.P., M.P.; funding acquisition, M.P., A.N.. All authors have read and agreed to the published version of the manuscript.

Funding: This research was funded by Marelli S.p. A.

Conflicts of Interest: The authors declare no conflict of interest.

References

1. Rozman, M.; Ikpehai, A.; Adebisi, B.; Rabie, K.; Gacanin, H.; Ji, H.; Fernando, M. Smart Wireless Power Transmission System for Autonomous EV Charging. *IEEE Access* **2019**, *7*, 112240–112248, doi:10.1109/access.2019.2912931.
2. Corti, F.; Reatti, A.; Pierini, M.; Barbieri, R.; Berzi, L.; Nepote, A.; De La Pierre, P. A Low-Cost Secondary-Side Controlled Electric Vehicle Wireless Charging System using a Full-Active Rectifier. In Proceedings of the 2018 International Conference of Electrical and Electronic Technologies for Automotive, Milan, Italy, 9–11 July 2018; pp. 1–6.

3. Pugi, L.; Reatti, A.; Mastromauro, R.A.; Corti, F. Modeling of inductive resonant transfer for electric vehicles. *Int. J. Electr. Hybrid Veh.* **2018,** *10*, 131–160.
4. Allotta, B.; Pugi, L.; Reatti, A.; Corti, F. Wireless power recharge for underwater robotics. *Int. J. Electr. Hybrid Veh.* **2018**, *10*, 131–160.
5. Standard SAEJ2954. A Wireless Power Transfer for Light-Duty Plug-In/Electric Vehicles and Alignment Methodology. Available online: https://www.sae.org/standards/content/j2954_201605/ (accessed on 10 December 2020).
6. Pugi, L.; Reatti, A.; Corti, F. Application of modal analysis methods to the design of wireless power transfer systems. *Meccanica* **2019**, *54*, 321–331, doi:10.1007/s11012-018-00940-x.
7. Tian, J.; Hu, A.P. A DC-Voltage-Controlled Variable Capacitor for Stabilizing the ZVS Frequency of a Resonant Converter for Wireless Power Transfer. *IEEE Trans. Power Electron.* **2017**, *32*, 2312–2318, doi:10.1109/tpel.2016.2559798.
8. Murliky, L.; Porto, R.W.; Brusamarello, V.J.; De Sousa, F.R.; Trivino-Cabrera, A.; Azambuja, R. Robust Active Tuning for Wireless Power Transfer to Support Misalignments and Variable Load. In Proceedings of the 2018 IEEE Wireless Power Transfer Conference (WPTC), Montreal, QC, Canada, 3–7 June 2018; pp. 1–4.
9. Wang, L.; Li, X.; Raju, S.; Yue, C.P. Simultaneous Magnetic Resonance Wireless Power and High-Speed Data Transfer System With Cascaded Equalizer for Variable Channel Compensation. *IEEE Trans. Power Electron.* **2019**, *34*, 11594–11604, doi:10.1109/tpel.2019.2916021.
10. Zheng, C.; Lai, J.-S.; Chen, R.; Faraci, W.E.; Zahid, Z.U.; Gu, B.; Zhang, L.; Lisi, G.; Anderson, D. High-Efficiency Contactless Power Transfer System for Electric Vehicle Battery Charging Application. *IEEE J. Emerg. Sel. Top. Power Electron.* **2015**, *3*, 65–74, doi:10.1109/jestpe.2014.2339279.
11. Duan, C.; Jiang, C.; Taylor, A.; Bai, K. Design of a zero-voltage-switching large-air-gap wireless charger with low electrical stress for Plugin Hybrid Electric Vehicles. In Proceedings of the 2013 IEEE Transportation Electrification Conference and Expo (ITEC), Detroit, MI, USA, 16–19 June 2013; pp. 1–5.
12. Lu, F.; Zhang, H.; Hofmann, H.; Mi, C. A high efficiency 3.3 kW loosely-coupled wireless power transfer system without magnetic material. In Proceedings of the 2015 IEEE Energy Conversion Congress and Exposition (ECCE), Montreal, QC, Canada, 20–24 September 2015; pp. 2282–2286.
13. Miller, J.M.; Onar, O.C.; Chinthavali, M. Primary-Side Power Flow Control of Wireless Power Transfer for Electric Vehicle Charging. *IEEE J. Emerg. Sel. Top. Power Electron.* **2015**, *3*, 147–162, doi:10.1109/jestpe.2014.2382569.
14. Li, S.; Li, W.; Deng, J.; Nguyen, T.D.; Mi, C. A Double-Sided LCC Compensation Network and Its Tuning Method for Wireless Power Transfer. *IEEE Trans. Veh. Technol.* **2014**, *64*, 2261–2273, doi:10.1109/tvt.2014.2347006.
15. Mai, R.; Liu, Y.; Li, Y.; Yue, P.; Cao, G.; He, Z.-Y. An Active-Rectifier-Based Maximum Efficiency Tracking Method Using an Additional Measurement Coil for Wireless Power Transfer. *IEEE Trans. Power Electron.* **2018**, *33*, 716–728, doi:10.1109/tpel.2017.2665040.
16. Wu, H.H.; Gilchrist, A.; Sealy, K.D.; Bronson, D. A High Efficiency 5 kW Inductive Charger for EVs Using Dual Side Control. *IEEE Trans. Ind. Inform.* **2012**, *8*, 585–595, doi:10.1109/tii.2012.2192283.
17. Corti, F.; Paolucci, L.; Reatti, A.; Grasso, F.; Pugi, L.; Tesi, N.; Grasso, E.; Nienhaus, M. A Comprehensive Comparison of Resonant Topologies for Magnetic Wireless Power Transfer. In Proceedings of the 2020 IEEE 20th Mediterranean Electrotechnical Conference (MELECON), Palermo, Italy, 16–18 June 2020; pp. 582–587.
18. Corti, F.; Grasso, F.; Paolucci, L.; Pugi, L.; Luchetti, L. Circular Coil for EV Wireless Charging Design and Optimization Considering Ferrite Saturation. In Proceedings of the 2019 IEEE 5th International forum on Research and Technology for Society and Industry (RTSI), Florence, Italy, 9–12 September 2019.